Original Article

Institution of MECHANICAL ENGINEERS
Journal of MECHANICAL ENGINEERING SCIENCE

Proc IMechE Part C:
J Mechanical Engineering Science
2016, Vol. 230(12) 2073–2085

DOI: 10.1177/0954406215588480
pic.sagepub.com
SAGE

Assessment of friction from compression ring conjunction of a high-performance internal combustion engine: A combined numerical and experimental study

M Gore[1], R Rahmani[2], H Rahnejat[2] and PD King[2]

Abstract

The paper presents direct measurement of in-cylinder friction from a single cylinder motocross race engine under motored conditions and compares the same with a new analytical predictive method. These conditions are encountered in piston–cylinder system with the application of cylinder deactivation (CDA) technology, which is a growing trend. The analytical method takes into account the various regions within instantaneous contact of compression ring–cylinder liner, including lubricant film rupture, cavitation zone and the subsequent lubricant film reformation. The analysis also includes the effect of boundary friction and lubricant rheology. The predictions and direct measurements of cyclic friction show good agreement and indicate dominance of viscous friction under the investigated engine running conditions. In particular, it is shown that the compression ring contribution to in-cycle friction is most pronounced in the region of high cylinder pressures because of combined Poiseuille friction and some boundary solid interactions. The combined experimental-analytical approach has not hitherto been reported in literature.

Keywords

In-cycle friction, floating liner, compression ring, viscous friction, boundary friction, cylinder deactivation

Date received: 16 December 2014; accepted: 27 April 2015

Introduction

The engine friction consumes around 7–8% of generated combustion energy in an internal combustion (IC) engine. Nearly half of these frictional losses are due to the piston system.[1,2] The frictional losses from the compression ring conjunction alone can amount for 3% of the total engine losses, which is quite significant for such a small component of the engine system.[3,4] With the combination of pervading global competition in the automotive sector, the rising fuel costs and ever stringent emission regulations, it is clear that these levels of parasitic losses are unsustainable. Therefore, a combination of verifiable methods of prediction and direct measurement of friction has to be sought so that the effect of any subsequent palliative measures may be accurately ascertained. The palliative approaches usually include the use of hard wear-resistant smooth coatings, cross-hatch honed cylinder liners and/or introduction of lubricant retaining textures in regions with poor lubricant entrainment such as at the piston dead centre reversals.[5–8]

Indirect measurement of friction is routinely performed through use of net indicated mean effective pressure (NIMEP).[2,3] However, the method is prone to inaccuracies. Therefore, floating liners have been developed to directly measure friction from engine test rigs. The principle of a floating liner was used by Furuhama and Sasaki,[9] based on a cylinder liner whose only connections to the bore were restricted through a set of intervening piezoelectric transducers. The inertial motion of the piston drags the liner, with the reaction measured by the transducers. The total reaction is equivalent to the net applied force on the liner due to gas pressure loading and the opposing friction. The principle of the operation and the system dynamics is fully explained by Gore et al.[10,11] A brief explanation of this is provided in the next section.

The compression ring–liner conjunction is a multi-parameter variate problem where a plethora of parameters affect the regime of lubrication, thus the

[1]Red Arch Engineering Ltd., Daventry, Northamptonshire, UK
[2]Wolfson School of Mechanical and Manufacturing Engineering, Loughborough University, Loughborough, Leicestershire, UK

Corresponding author:
R Rahmani, Wolfson School of Mechanical and Manufacturing Engineering, Loughborough University, Loughborough, Leicestershire, UK.
Email: R.Rahmani@lboro.ac.uk

generated friction. There have been many predictive numerical analyses with varying degrees of complexity. The basic approach assumes good circumferential ring-bore conformance. This enables the solution of Reynolds equation (as the hydrodynamic governing equation) in one dimension with an analytical approach. Haddad and Tjan[12] show that such a simplification can be assumed with good ring-bore peripheral conformance and crucially the fitted ring's perimeter-to-face width ratio being greater than 30 (assumed long line sliding contact). With this method other salient features such as the effect of surface topography can also be included within an analytical solution,[13] thus not resulting in long computation times. For example, Sawicki and Yu[14] provide such a solution, incorporating the effect of lubricant cavitation which affects both the load-carrying capacity and generated friction.

Morris et al.[15] provide an alternative analytical solution which makes use of average flow model representation of Reynolds equation, including the effect of surface topography in the prediction of viscous friction with the addition of boundary contribution, based on the approach of Greenwood and Tripp.[16] Morris et al.[17] and Shahmohamadi et al.[18] also included a control volume thermal mixing model to take into account the effect of lubricant shear heating as well as surface temperature of the contiguous solids (liner and the ring); the latter using a computational fluid dynamics approach. This predicts more realistic lubricant viscosity, thus generated friction. Another tribodynamic analysis including the effect of generated temperature for the high-pressure region around the top dead centre (TDC) reversal from compression to power stroke was recently provided by Mishra.[19] A combined solution of Reynolds and energy equations was made.

The engine used in the current investigation is a high-performance spark ignition single-cylinder motocross motorbike engine, which uses a single compression ring of 1.15 mm face width. The floating liner has a bore of 96 mm; thus a fully fitted ring has a perimeter of 301.1 mm, with a fitted end gap of 0.4 mm. The perimeter-to-face width ratio is in excess of 262, justifying the use of one-dimensional sliding analysis. In practice, however, the bore is out-of-round[20] although every effort is made for the current floating liner to closely approximate an idealised right circular cylindrical shape. Furthermore, the ring is subjected to variable chamber pressure loading,[21] thus in reality ring dynamic occurs,[22–24] which would ideally require a lengthy two-dimensional solution such as those developed in Ma et al.,[25] Bolander et al.[26] and Mishra et al.[27,28] Nevertheless, for the conditions described in this paper a one-dimensional analytical solution is quite adequate and shows good conformance to the measurements. In fact, such a combined analytical-experimental approach has not hitherto been reported in literature.

It should be noted that the results in this study are for motored running conditions. For the engine used the results are applicable to fired conditions with up to 30% throttle for cold running conditions. The engine testing time for in situ measurement is also kept short, typically 15 min in order to guard against any significant rise in the liner temperature, thus enabling a reasonable comparison between the predictions based upon an isothermal analytical method and the measured results. It is also applicable to deactivated cylinders in the growing trend in the use of partially deactivated engines in urban driving conditions.

The engine test-bed

A Honda CRF 450R motocross motorcycle 4-stroke engine with the maximum speed of 11,000 r/min was chosen because of its high power and torque characteristics (41 kW, 50 Nm). The load–speed combination envelopes a wide range of engine technology. In fact, it is representative of the highest performing naturally aspirated single cylinder engine technology (i.e. over 90 kW/L and 110 Nm/L). The engine's original engine manufacturer (OEM) barrel was replaced by a wet barrel, containing the floating liner. Due to the differential operating temperature, there is a need to control the clearance between the cylinder liner and the housing, thus minimising the induced stresses in the OEM aluminium structure. The choice of housing material was restricted to materials with a coefficient of thermal expansion between 16 and 18 ppm/K, and yield strength significantly higher than the original OEM engine barrel. Thus, austenitic stainless steel grade 304 was used for the floating liner (Figure 1). The working surface of the liner is coated with a 60 μm thick Ni–SiC layer. As shown, the floating liner is suspended in such a way that any point of contact between the liner and any rigidly mounted components are intervened by a number of piezoelectric load cells.[10,11] The load cells are preloaded whilst in situ and at rest, including the weight of the liner itself. The preload value is obtained and recorded prior to any testing. Thereupon, the readings of all the load cells are set to zero prior to any testing. This means that the values obtained during any testing represent the dynamic changes only. The infinitesimal movement of the liner is such that the load cells remain perpetually in compression. The total load cell readings equate the inertial force of the liner, dragged by the motion of the piston. The net applied force is due to gas pressure loading on the upper rim of the liner, which is sealed by a labyrinth seal and liner–piston friction. Thus, depending on the sense of liner motion the friction is measured directly as

$$\pm f = Ma_l - P_s \tag{1}$$

The engine was mounted onto an Oswald 250 kW transient dynamometer. All standard engine testing

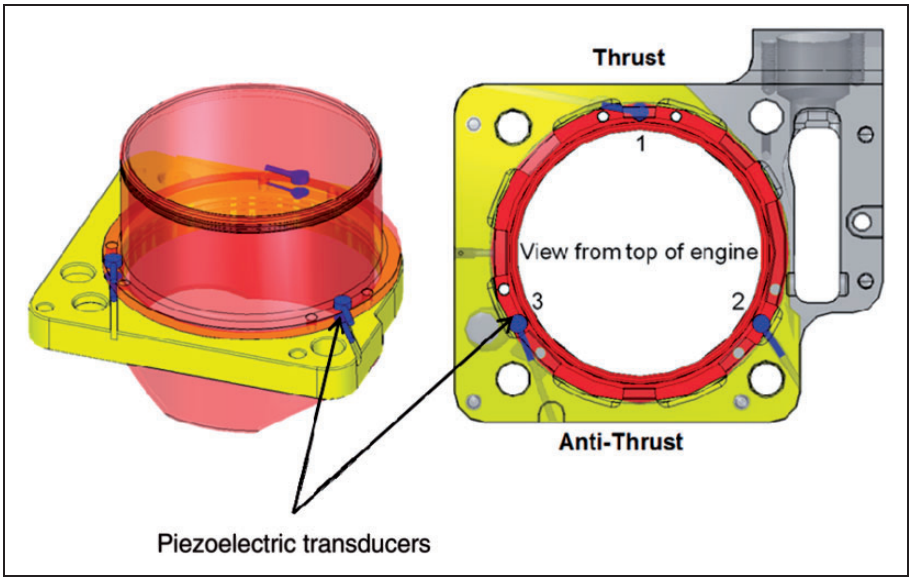

Figure 1. The floating liner (after Gore et al.[11]).

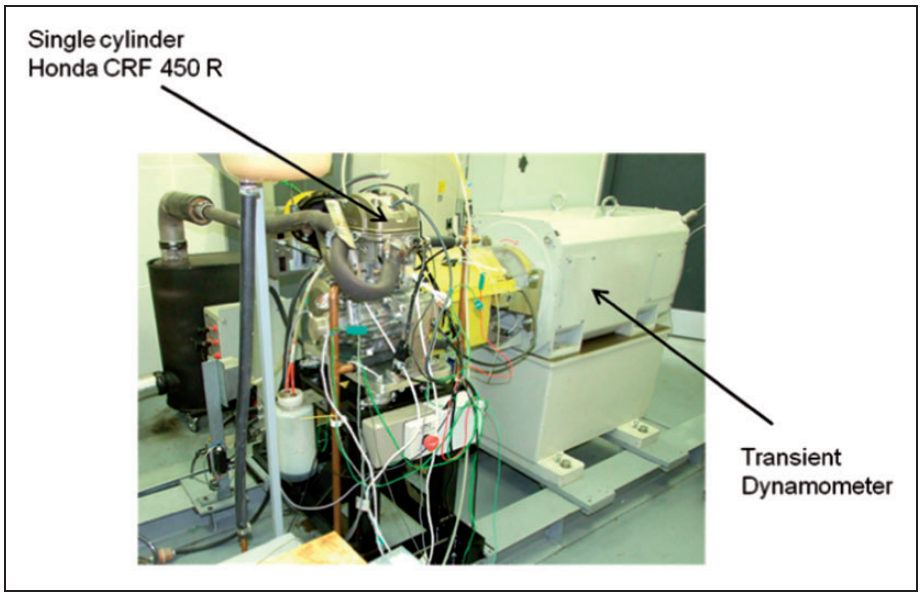

Figure 2. The engine test-bed.

parameters (chamber pressure, air fuel ratio, test cell humidity, test cell temperature, input temperature of fuel and coolant, etc.) were logged as well as friction to ensure reliability and consistency of all measurements. The basic setup is shown in Figure 2. Further details are given by Gore et al.[10,11]

Analytical predictive method

With the aforementioned assumptions of good ring–liner conformability and large ring perimeter-to-face width ratio, Reynolds equation in one-dimensional flow along the ring face width becomes

$$\frac{\partial}{\partial x}\left(\frac{\rho h^3}{6\eta}\frac{\partial p}{\partial x} - \rho U h\right) = \frac{\partial(2\rho h)}{\partial t} \tag{2}$$

where U denotes the piston sliding velocity.

This form of Reynolds equation assumes no side leakage of the lubricant in the lateral (circumferential) direction to that of lubricant entrainment. This assumption is justified as the ring–liner conjunction enjoys a thin lubricant film.

Therefore, the lubricant entrainment occurs along the ring face width, x in a domain characterised by

$$x \in [a, b] \quad \text{where, } a \leqslant c < r \leqslant b \tag{3}$$

The parameters a, c, r and b represent the contact inlet, lubricant film rupture point (onset of cavitation region), lubricant reformation boundary and the outlet edge of the ring face width, respectively (see Figure 3). These positions demarcate regions of

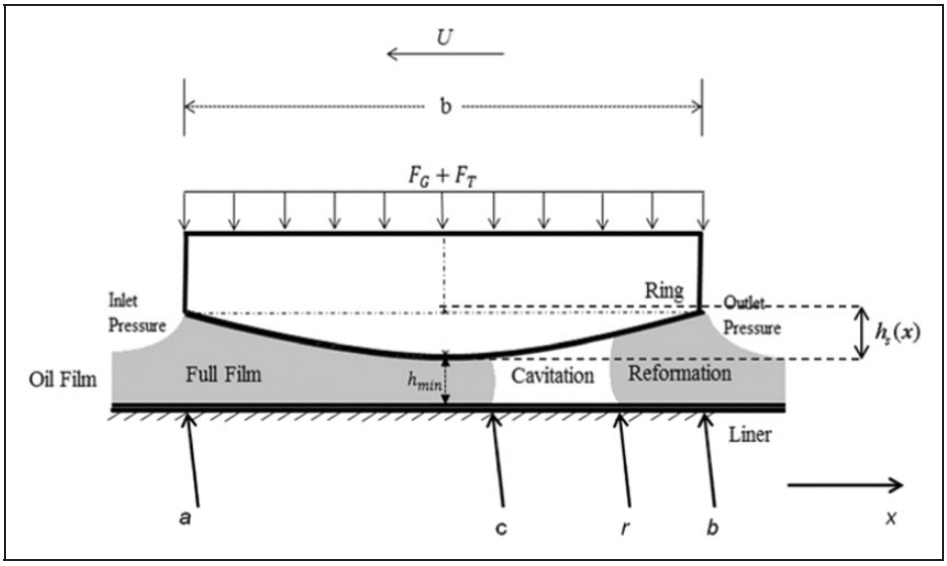

Figure 3. Lubricant film variation within the contact domain.

assumed full film, cavitation and lubricant film reformation.

Reynolds equation has to be solved simultaneously with the film shape function in a transient manner

$$h(x,t) = h_{min}(t) + h_s(x) \tag{4}$$

where $h_s(x) = x^2/2R$ is the parabolic shape of the ring face width profile.

The appropriate boundary conditions for solution of Reynolds equation are

$$\begin{cases} p\big|_{x=a} = P_a \quad (I) \\ p\big|_{x=c} = P_c \quad (II) \\ \frac{\partial p}{\partial x}\big|_{x=c} = 0 \quad (III) \\ p\big|_{x=r} = P_r = P_c \quad (IV) \\ p\big|_{x=b} = P_b \quad (V) \end{cases} \tag{5}$$

The inlet pressure P_a varies according to the sense of motion of the piston (Condition (I)). In the upstroke, it is the combustion chamber pressure, whilst in the downstroke it is the inter-ring pressure, which is considered to be the atmospheric pressure in the current study. The lubricant film ruptures at a position $x = c$, where the lubricant pressure falls below its cavitation vaporisation pressure P_c (Condition (II)). At this location, the third boundary condition in equation (5) is also taken into account which ensures flow continuity (Condition (III)). The second and third boundary conditions, taken together, are known as the Swift–Stieber boundary conditions. The pressure remains the same in the cavitation region, and gradually rises to that prevailing at the lubricant exit boundary edge of the ring (Conditions (IV) and (V)). These induce lubricant film reformation.

The solution of Reynolds equation has to take into account three different regions in the contact domain as shown in Figure 3 as further explained below.

Region of full film ($a \leqslant x \leqslant c$)

Two successive integrations of Reynolds equation with respect to x yields

$$\begin{aligned} p = {} & 6U\int_a^x \frac{\eta}{h^2}\mathrm{d}s + 12\int_a^x \left(\frac{\eta}{\rho h^3}\int_a^s \frac{\partial(\rho h)}{\partial t}\mathrm{d}s'\right)\mathrm{d}s \\ & + 6C_1\int_a^x \frac{\eta}{\rho h^3}\mathrm{d}s + C_2 \end{aligned} \tag{6}$$

Now using the boundary conditions (I) and (III) yields the integration constants

$$C_1 = \frac{(P_c - P_a) - \left[6U\int_a^c \frac{\eta}{h^2}\mathrm{d}x + 12\int_a^c \left(\frac{\eta}{\rho h^3}\int_a^x \frac{\partial(\rho h)}{\partial t}\mathrm{d}s\right)\mathrm{d}x\right]}{6\int_a^c \frac{\eta}{\rho h^3}\mathrm{d}x}$$

$$\text{and } C_2 = P_a \tag{7}$$

Therefore, the pressure distribution in the full film region of the contact is determined by replacing for constants of integration C_1 and C_2 from equation (7) into equation (6) in terms of the film rupture position $x = c$, which is unknown. This position can be determined at any given time (crank angle position), using the boundary condition (III) in equation (5)

$$\begin{aligned} & 6U + \frac{12}{\rho_c h_c}\int_a^c \frac{\partial(\rho h)}{\partial t}\mathrm{d}s \\ & + \frac{(P_c - P_a) - \left[\begin{array}{l} 6U\int_a^c \frac{\eta}{h^2}\mathrm{d}x \\ \quad + 12\int_a^c \left(\frac{\eta}{\rho h^3}\int_a^x \frac{\partial(\rho h)}{\partial t}\mathrm{d}s\right)\mathrm{d}x \end{array}\right]}{6\int_a^c \frac{\eta}{\rho h^3}\mathrm{d}x} = 0 \end{aligned} \tag{8}$$

Equation (8) is solved by Newton–Raphson iterations to determine the position $x = c$. Note that both P_a and U are functions of the crank angle location in an engine cycle. P_a is a function of chamber pressure or is simply atmospheric in the downstroke sense of the piston and the sliding speed U is given as[29]

$$U(\varphi) = r_{cr}\omega\left(\sin\varphi + \frac{r_{cr}}{2\ell}\sin 2\varphi + \ldots\right) \tag{9}$$

The film reformation region ($r \leqslant x \leqslant b$)

Reynolds equation (2) is doubly integrated again between the limits r and b

$$p = 6U\int_r^x \frac{\eta}{h^2}\mathrm{d}s + 12\int_r^x\left(\frac{\eta}{\rho h^3}\int_r^s \frac{\partial(\rho h)}{\partial t}\mathrm{d}s'\right)\mathrm{d}s + 6C_3\int_r^x \frac{\eta}{\rho h^3}\mathrm{d}s + C_4 \tag{10}$$

Applying the boundary conditions (IV) and (V) yields the integration constants

$$C_3 = \frac{(P_b - P_r) - \left[6U\int_r^b \frac{\eta}{h^2}\mathrm{d}x + 12\int_r^b\left(\frac{\eta}{\rho h^3}\int_r^x \frac{\partial(\rho h)}{\partial t}\mathrm{d}s\right)\mathrm{d}x\right]}{6\int_r^b \frac{\eta}{\rho h^3}\mathrm{d}x}$$

$$\text{and } C_4 = P_r \tag{11}$$

The conjunctional outlet pressure P_b depends on the sense of piston motion, in the same manner as the inlet pressure P_a. However, constant C_3 can only be calculated if the film reformation position, r can be determined. For this purpose, the conditions in the cavitation region should be considered.

The cavitation region ($c \leqslant x \leqslant r$)

In the cavitation region the pressure is assumed to be constant at the lubricant vaporisation pressure, P_c[14] with the density of lubricant being a function of pressure and its bulk modulus as[30]

$$\beta = \rho\frac{\partial p}{\partial \rho} \tag{12}$$

The ratio of density in the cavitated region to that in the full film region of the contact is defined as the film ratio, $\theta = \rho/\rho_c$, where lubricant density and viscosity vary with pressure and temperature (see the next section).

As the result of constant pressures in the cavitation region, striated flow only proceeds in moderate to highly loaded contacts, mainly due to viscous shear (Couette flow).[31] This means that the Poiseuille (pressure-induced) flow in Reynolds equation may be neglected in this region. Therefore, Reynolds equation can be altered to the form, initially proposed by Elrod[31] in terms of θ as

$$\frac{\partial}{\partial x}\left(\frac{\rho_c h^3}{6\eta}g\beta\frac{\partial\theta}{\partial x} - U\rho_c\theta h\right) = 2\frac{\partial(\rho_c\theta h)}{\partial t} \tag{13}$$

where pressure is replaced by the film ratio as

$$p = g\beta\ln\theta + P_c \tag{14}$$

And g is defined as switching term

$$g = \begin{cases} 1 & \textit{in the full film region} \\ 0 & \textit{in the cavitated region} \end{cases} \tag{15}$$

In the cavitation region with viscous shear flow only, the equation above reduces to

$$U\frac{\partial(\theta h)}{\partial x} + 2\frac{\partial(\theta h)}{\partial t} = 0 \tag{16}$$

De la Cruz et al.[32] observed that the value of θ alters in the cavitation region according to the approach or separation of surfaces, as indicated by the second term in equation (16), where a negative value indicates approach of the surfaces. Equation (16) is essentially a first-order partial differential equation which can be solved using the method of characteristics. Sawicki and Yu[14] show that

$$(\theta h)_{x=c,t_c} = (\theta h)_{x=r,t_r} \tag{17}$$

where, t_c and t_r are the times at which film rupture and reformation occur.

At the film rupture point: $\theta_{x=c} = \theta_c = 1$, which using equation (17) leads to

$$\theta_{x=r} = \theta_r = \frac{h_{c,t_c}}{h_{r,t_r}} \tag{18}$$

This, together with equation (14) fully describes the cavitation region of the flow. The only remaining unknown is the constant of integration C_3 in equation (11), which depends on the position at the onset of film reformation. Using the boundary conditions of equation (5) in the Elrod's equation (13), it follows that

$$\begin{cases} p\big|_{x=r} = P_r = P_c \\ \left.\dfrac{\partial p}{\partial x}\right|_{x=r} = \dfrac{12\eta_r}{h_r^2}\left(\dfrac{U}{2} - \dfrac{\mathrm{d}r}{\mathrm{d}t}\right)(1-\theta_r) \text{ where } \theta_r = \dfrac{\rho_r}{\rho_c} \end{cases} \tag{19}$$

At the start of reformation region, r, this also must equate to the pressure gradient for the

reformation region in the previous sub-section, obtained as

$$\frac{\partial p}{\partial x} = \frac{6\eta}{\rho h^3}\left(\rho U h + 2\int_r^x \frac{\partial(\rho h)}{\partial t}\mathrm{d}x + C_3\right) \tag{20}$$

Equating (19) and (20) and replacing for θ_r from equation (18) and after some basic manipulations

$$C_3 = \rho_r h_r\left[\left(\Delta U - 2\frac{\mathrm{d}r}{\mathrm{d}t}\right)\left(1 - \frac{h_{c,t_c}}{h_{r,t_r}}\right) - U\right] \tag{21}$$

Replacing for C_3 in equation (11) enables the evaluation of the rupture point r from the equation below using Newton–Raphson iterations

$$\left(U - 2\frac{\mathrm{d}r}{\mathrm{d}t}\right)\left(1 - \frac{h_{c,t_c}}{h_{r,t_r}}\right) = U + \frac{(P_b - P_r) - \left[\begin{array}{l} 6U\int_r^b \frac{\eta}{h^2}\mathrm{d}x \\ \quad + 12\int_r^b \left(\frac{\eta}{\rho h^3}\int_r^x \frac{\partial(\rho h)}{\partial t}\mathrm{d}x\right)\mathrm{d}x \end{array}\right]}{6\rho_r h_r \int_r^b \frac{\eta}{\rho h^3}\mathrm{d}x} \tag{22}$$

Lubricant rheology

Lubricant density and viscosity alter with pressure and temperature. The density variation with pressure and temperature in the full film region is given by Dowson and Higginson[33] and Yang et al.[34]

$$\rho = \rho_0(1 - \gamma\Delta T)\left[1 + \frac{6\times 10^{-10}(p - P_{atm})}{1 + 1.7\times 10^{-9}(p - P_{atm})}\right] \tag{23}$$

where γ is the thermal expansion coefficient for the lubricant. It is usually considered to be around $6.4\times 10^{-4}\mathrm{K}^{-1}$.[32,33] Morris et al.[17] showed that the rise in lubricant temperature occurs at the inlet to the contact by the contiguous surfaces convecting heat into the entrant bulk lubricant. Therefore, ΔT can be taken as the difference between the liner temperature and the bulk oil temperature, measured from the engine sump (i.e. $\Delta T = T - T_0$). The liner temperature and that of the ring are assumed to be the same, although in practice the moving surface has a slightly higher temperature.[17] In the cavitation region, the density is obtained from equation (23) and the film ratio θ.

Lubricant viscosity alters with temperature more significantly than its density in moderately loaded contacts such as the ring–bore conjunction. According to Houpert[35]

$$\eta = \eta_0 \exp\left\{[\ln(\eta_0) - \ln(\eta_\infty)] \times \left[\left(\frac{T - 138}{T_0 - 138}\right)^{-S_0}\left(1 + (p - P_{atm})/C_p\right)^Z - 1\right]\right\} \tag{24}$$

where Z and S_0 are constants, independent of temperature and pressure

$$Z = \frac{\alpha_0}{[\ln(\eta_0) - \ln(\eta_\infty)]/C_p} \text{ and } S_0 = \frac{\beta_0(T_0 - 138)}{\ln(\eta_0) - \ln(\eta_\infty)} \tag{25}$$

and, $C_p = 1.98\times 10^8$ Pa and $\eta_\infty = 6.31\times 10^{-5}$ Pa.s.

Contact load and friction

Disregarding any ring elastodynamic behaviour described by Baker et al.,[24] the instantaneous contact load is a quasi-static balance between the applied load to the ring and the contact reaction. The applied forces include the ring tension force, F_T, which strives to return the ring to its unfitted state, as the result adhering it to the liner surface (Figure 3). Additionally, the chamber pressure acts behind the inner rim of the compression ring and acts outwards as the gas force, F_G, also orthogonal to the contact surface. The summation of these forces constitutes the instantaneous applied contact load as

$$F = F_T + F_G \tag{26}$$

It is assumed that 100% of the chamber pressure acts behind the compression ring, which fully conforms circumferentially to the liner surface with the footprint contact area of $A = 2\pi r_0(b - a)$, r_0 being the radius of an idealised liner of right circular cylindrical shape, and P_G is the chamber pressure. Therefore

$$F_G = P_G A \tag{27}$$

The ring tension force is

$$F_T = P_e A \tag{28}$$

where the uniform elastic pressure P_e is[36]

$$P_e = \frac{GEI}{3\pi(b - a)r_0^4} \tag{29}$$

where G is the end-gap of the incomplete circular compression ring in its free state.

The net applied force on the ring towards the liner surface is balanced by the contact reaction, comprising the hydrodynamic load-carrying capacity as the result of generated lubricant pressures and any

direct contact of surface asperities. The hydrodynamic reaction is

$$W_h = 2\pi r_0 \int_{x=a}^{b} p\mathrm{d}x \tag{30}$$

Note that the low pressures in the cavitation and lubricant film reformation regions do not appreciably contribute to lubricant hydrodynamic reaction.

A small area of asperity contact can occur in the compression ring–liner contact, particularly at piston dead centre reversals with low values of U, thus low entrainment flow of lubricant into the conjunction.[13] The area of asperity contact is a tiny fraction of the apparent contact area A, described above. If a Gaussian distribution of asperities is assumed, then the proportion of contact load carried by them may be obtained, using Greenwood and Tripp[16] approach, where the asperity contact area and their share of carried load respectively become

$$A_a = \pi^2(\zeta\kappa\sigma)^2 A F_2(\lambda) \tag{31}$$

$$W_a = \frac{16\sqrt{2}}{15}\pi(\zeta\kappa\sigma)^2\sqrt{\frac{\sigma}{\kappa}}E' A F_{5/2}(\lambda) \tag{32}$$

The statistical functions $F_2(\lambda)$ and $F_{5/2}(\lambda)$ relate to the Gaussian distribution of asperities and are functions of the Stribeck oil film parameter defined as $\lambda = h_{min}(t)/\sigma$, where σ is the standard deviation of composite surface roughness of the counterface surfaces. These functions can be represented by the fitted polynomial functions of λ and diminish as $\lambda \to 3$ (purely hydrodynamic condition)[37]

$$F_2(\lambda) = -0.0018\lambda^5 + 0.0281\lambda^4 - 0.1728\lambda^3 + 0.5258\lambda^2 - 0.8043\lambda + 0.5003 \tag{33}$$

$$F_{5/2}(\lambda) = -0.0046\lambda^5 + 0.0574\lambda^4 - 0.2958\lambda^3 + 0.7844\lambda^2 - 1.0776\lambda + 0.616 \tag{34}$$

It is noteworthy that the usual cylinder liner configuration is cross-hatch honed. In such cases, the surface topography does not follow a Gaussian distribution of asperities as it forms a plateau. This makes a comparison between analytical predictions and measured results quite complicated. Therefore, for the case of the floating liner in this study a super-finished liner surface is made. For the usual cross-hatched liners the height of the plateau $\sigma = R_k$ is used, whereas in the current study $\sigma = R_q$ is appropriate and a Gaussian distribution of asperities is assumed. The surface topography is measured, using an infinite focus white light interferometer with a nominal measurement resolution of 1 nm. The procedure followed is described in detail in Styles et al.[38]

The total contact reaction is, therefore

$$W = W_h + W_a \tag{35}$$

As already mentioned, there are two contributing sources to conjunctional friction: Firstly, the reported literature shows that for most of the engine cycle, the dominant mechanism of friction is viscous shear of the lubricant. Secondly, in the regions of piston motion with low sliding velocity (at or in the vicinity of motion reversals) there is lack of sufficient lubricant entrainment into the contact conjunction (low value of U). In these locations two other sources of friction play an important role. One is due to the direct contact of counterface surface asperities (boundary lubrication). The combination of boundary and viscous friction leads to a mixed regime of lubrication. The other mechanism is pressure-induced viscous shear (Poiseuille shear), which occurs with a rise in pressure gradient across the conjunction ($\mathrm{d}p/\mathrm{d}x$). This can occur at piston reversals, particularly at the top dead centre and in transition from the compression stroke to the power stroke. All these sources of friction should be taken into account. For lubricant contributions

$$f_v = \tau_v(A - A_a) \tag{36}$$

where

$$\tau_v = \pm\frac{h}{2}\left(\frac{\mathrm{d}p}{\mathrm{d}x}\right) + \frac{\eta U}{h} \tag{37}$$

The contribution due to asperity interactions occurs over the area of asperity peaks A_a. There are two contributions in this case: One is due to adhesive friction of cold welded asperities under localised pressure which is shown by the second term on the right-hand side of equation (38). Here, the coefficient of asperity shear strength, ς is analogous to the coefficient of friction at the asperity-level contact and is usually measured through use of atomic force microscopy (AFM) in contact mode.[38,39] The second contribution is the first term in equation (38), which is based on the assumption that an ultra-thin film of lubricant is adsorbed to the asperity tips and undergoes non-Newtonian shear at its limiting Eyring shear stress, τ_0.[40]

$$f_b = \tau_0 A_a + \varsigma W_a \tag{38}$$

The asperity contacts can also cause elasto-plastic deformation, which affect boundary friction. These are not taken into account, but are indirectly accounted for by the direct measurement of ς. The value of ς corresponds to the coating of the cylinder liner which is Ni–SiC. This is obtained through use of an AFM, operating in lateral force mode as fully described by Styles et al.[38,39] More comprehensive

models for asperity level friction have recently been developed.[41,42]

Finally, the total friction is

$$f = f_v + f_b \tag{39}$$

Therefore, the predicted and measured frictions from equations (1) and (39) can be compared.

Solution method

The following solution procedure is followed:

Step 1: At the initial crank angle (time), an initial value for the hydrodynamic pressure distribution enables calculation of the corresponding rheological parameters from 'Lubricant rheology' section. In addition, an initial value for the minimum film thickness, h_{min} and squeeze film velocity dh/dt, is assumed. These values are subsequently altered during the iteration process.

Step 2: The pressure distribution is calculated ('Analytical predictive method' section).

Step 3: The rheological properties of lubricant are updated based on the pressure distribution from Step 2. This step is repeated until the following convergence criterion is met

$$\frac{\sum_{i=0}^{N} |p_i^{new} - p_i^{old}|}{\sum_{i=0}^{N} (p_i^{new})} < 10^{-4} \tag{40}$$

Step 4: The final hydrodynamic pressure distribution is integrated over the entire contact area (equation (30)). The asperity load support is also calculated from equation (32).

Step 5: The instantaneous applied contact load is obtained from equations (26) to (29).

Step 6: Instantaneous quasi-static equilibrium at a given crank angle demands that the following convergence criterion is satisfied

$$\frac{|W - F|}{F} < 10^{-3} \tag{41}$$

Otherwise, a new minimum film thickness value is calculated from

$$h_{min}^{new} = h_{min}^{old} \left[1 + \chi \left(\frac{W - F}{F} \right) \right] \tag{42}$$

where the numerical damping factor was considered to be $\chi = 0.075$ for optimum trade-off between solution stability and computation time.

Then, Steps 2 to 6 are repeated until the condition (41) above is satisfied.

The calculation process continues until a periodic minimum film thickness variation is achieved for the whole engine cycle.

Results and discussion

In practice, it is difficult to isolate the frictional losses from a particular conjunction (such as that of the compression ring–liner contact) in an IC engine.

Firstly, unlike multi-cylinder configuration, in single cylinders the contribution to frictional losses is quite significant in the case of engine bearings.[43] Consequently, the single cylinder engine used in this investigation uses rolling element bearings as its big-end bearing, which significantly reduces the

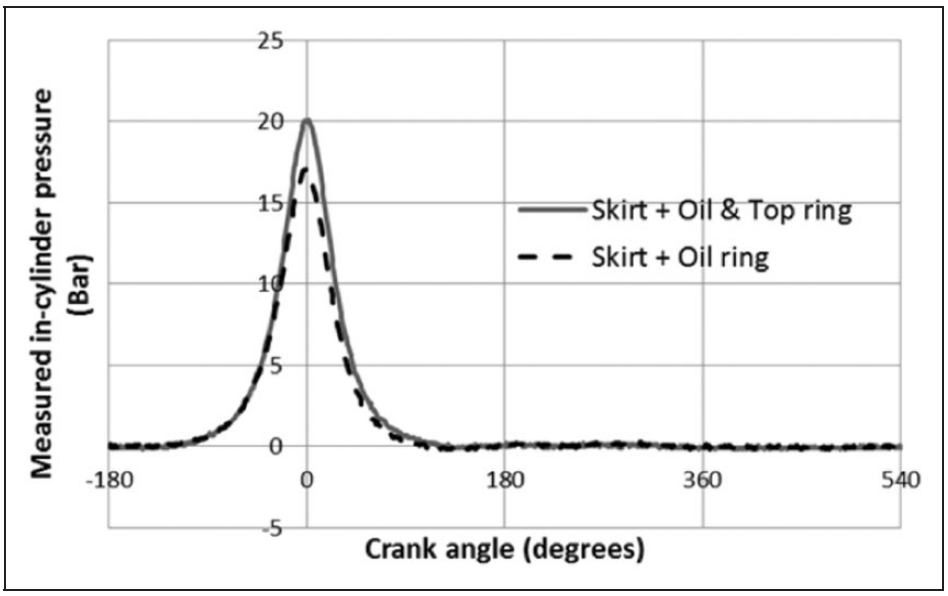

Figure 4. Cylinder chamber pressure for motored engine at 3000 r/min.

Table 1. List of engine specifications and employed data.

Parameter	Value	Unit
Engine speed	3000	r/min
Connection rod length	107	mm
Engine stroke	62.1	mm
Liner base material	Steel	–
Liner coating material	Ni–SiC	–
Bore nominal radius	48	mm
Top ring material	Steel	–
Liner elasticity modulus	203	GPa
Liner Poisson's ratio	0.3	–
Ring elasticity modulus	203	GPa
Ring Poisson's ratio	0.3	–
Ring end gap	10.5	mm
Ring face width	1.15	mm
Coefficient of asperity shear strength	0.22	–
Ra for liner surface	0.515	μm
Ra for ring surface	0.201	μm
Combined roughness parameter ($\eta\beta\sigma$)	0.0771	–
Combined roughness parameter (σ/β)	0.211	–
Operating temperature	25	°C
Oil density at 15°C	833.8	kg/m^3
Oil viscosity at 40°C	50	mPa.s
Thermal expansion coefficient	6.4×10^{-4}	K^{-1}
Pressure–viscosity coefficient, α_0	1×10^{-8}	Pa^{-1}
Temperature–viscosity coefficient, β_0	0.04	K^{-1}

generated friction when compared with the usual elliptic bore journal bearing. This is another reason for the choice of Honda CRF 450R engine for this study.

Secondly, direct measurement of in situ friction requires a floating liner, described in The Engine Test-bed Section. A somewhat over-sized piston, providing a nominal clearance of 50 μm was specifically produced in order to be able to remove the top compression ring and measure friction of the piston skirt and oil control ring assembly alone under motored conditions. Such a test is not possible under fired conditions. The difference between the friction of full piston assembly (with the compression ring included) and that without it, is assumed to yield the frictional contribution of the compression ring. Fortunately, with the Honda CRF 450R, the chamber pressure reaches a maximum value of 20 bar at the top dead centre without cylinder firing (Figure 4). This is quite representative of chamber pressure for fired condition at 30% throttle at the same engine speed of 3000 r/min. This has the added advantage of eliminating other phenomena under fired conditions, such as piston and liner thermo-elastic distortion. Therefore, the motorised testing in line with the above stated conditions reported here can also provide representative conditions for fired engine conditions at cold start-up.

Table 1 lists the engine specifications and all the data used as the input to the analysis. Note that the maximum cylinder pressure occurs at the top dead centre under motored condition and is slightly lower without the presence of the top compression ring because the cylinder chamber is not completely sealed, even with a slightly *over-sized* piston.

Figure 5(a) shows the measured friction using the floating liner's piezo-electric transducers, chamber pressure curves in Figure 4 and equation (1). The changes of sign in friction represent piston reversals. The gap between the two traces can be attributed to the frictional contribution of the compression ring. The results show that the main contribution to friction in the case of this engine set up and running conditions is due to the piston skirt and oil ring. For the test conditions reported here (Table 1), the compression ring friction contribution is approximately 10–15% of the total (Figure 5). Since the conditions with or without the compression ring in place are not identical (e.g. different in-cylinder pressures) and there is a certain amount of *noise* resident on the friction traces, the signals cannot reliably be subtracted.

Figure 5(b) shows the predicted friction during an engine cycle under the same conditions as those in Figure 5(a). The variations in the sliding velocity are also shown in the figure. The first thing to note is that friction variation is directly proportional to the sliding velocity (i.e. $f \propto U$), indicating that Couette shear of the lubricant film is the dominant responsible mechanism for friction (see second term on the right-hand side of equation (37)). This proportionality is lost in the region of rising chamber pressures prior to the TDC and proceeds further into the last stages of expansion stroke (corresponding to the power stroke in a fired engine). However, this rise in friction cannot entirely be attributed to the boundary friction effect as examining the variations of the minimum film thickness shown in Figure 6 indicates that the minimum film thickness barely falls below the mixed regime of lubrication (the demarcation boundary: $\lambda = 3$ line in Figure 6). In fact only in a very small part of the aforementioned compression-to-intake region some asperity interactions occur. This highlights the contribution from the pressure-induced shear (Poiseuille shear) as shown by the first term on the right hand side of equation (37). Therefore, in the case of a motored engine, where a sufficient supply of lubricant is available on the liner at the TDC reversal, the shear induced by pressure gradient at the end of the compression stroke and start of the expansion stroke can be quite significant.

Figure 5(c) and (d) shows the compression ring–liner friction contributions in two regions.

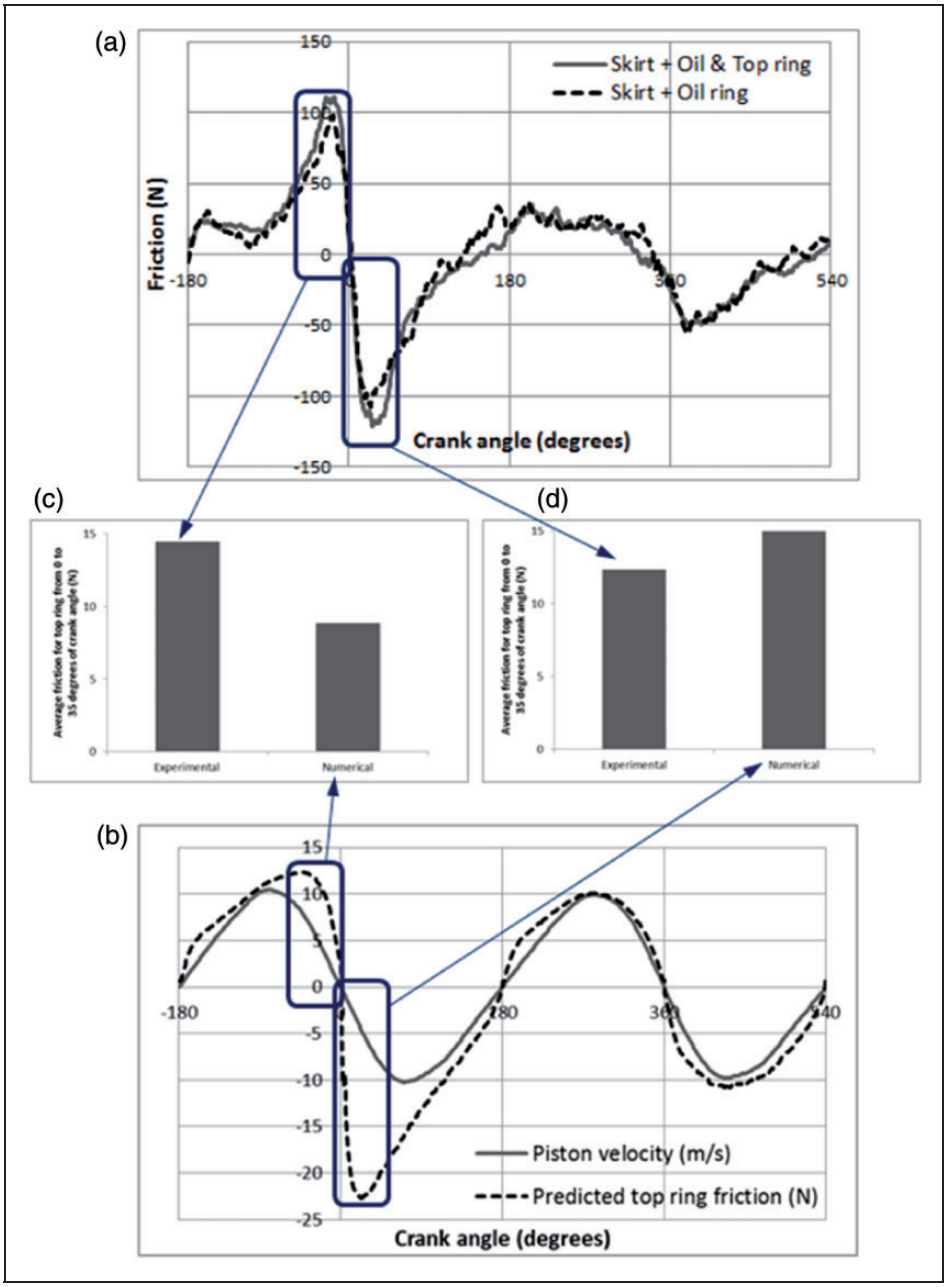

Figure 5. Comparison of measured and predicted ring–liner friction.

One region is in the compression part of the cycle, prior to the TDC reversal at the crank angle of 0° and the other is in the early stages of the expansion stroke, past the same TDC reversal. An average value for each region is calculated from measurements and predictions. These are shown in Figure 5(c) and (d).

Reasonably good agreement is demonstrated. However, there are some residual differences which can be attributed to many causes. These may include some of the assumptions of the analytical method used, such as ring–liner circumferential conformity, ignoring the piston (and ring) dynamics, assumed isothermal conditions and/or a fully flooded conjunctional inlet. Although the engine is motored and the test duration does not exceed 15 min, the viscous shear of the lubricant can promote a rise in its temperature and that of the adjacent solid boundaries. Therefore, the isothermal analysis here can lead to a certain degree of error. Furthermore, in practice a fully flooded inlet in the upstroke sense of the engine is not likely, and such an assumption can be regarded as idealised. On the experimental side the presented results are average of many cycles, where there are small variations (1–2%) in chamber pressure. In addition, the position of TDC reversals can alter from cycle to cycle, this being a characteristic of inherently unbalanced

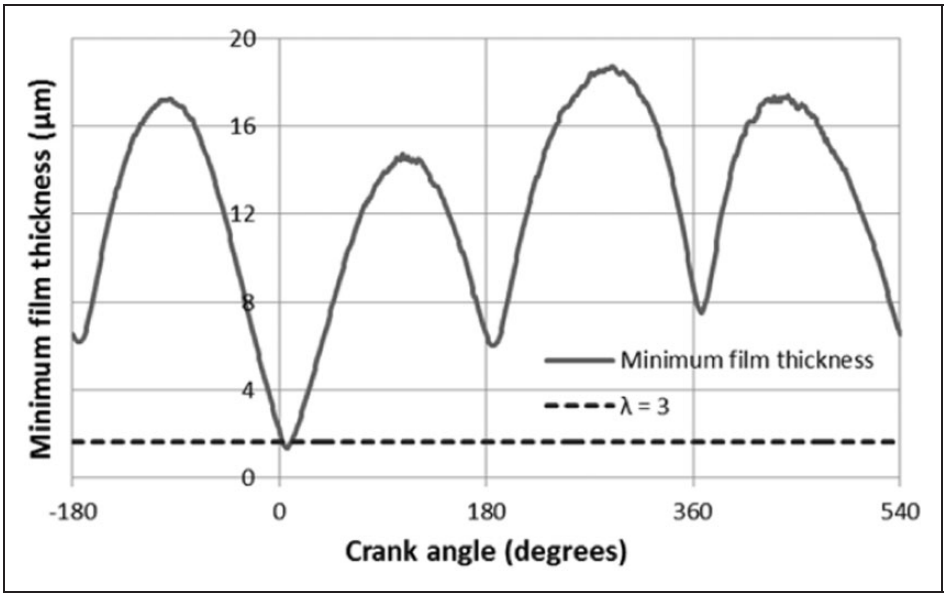

Figure 6. Variations of minimum film thickness for one engine cycle.

single cylinder engines.[29] Nevertheless, there is generally good overall agreement between measurements and predictions.

Conclusions

The paper presents direct in situ measurement of in-cylinder friction using a devised floating liner system. With a slightly over-sized piston, it was possible to remove the compression ring in the single cylinder motocross motor-cycle engine. The difference in the cyclic frictional traces with and without the presence of the compression ring provided an assessment of in-cycle friction contributed by the compression ring. An analytical predictive method, based on Elrod's modification to Reynolds equation, taking into account the effect of film reformation is also presented. The predicted viscous friction using this approach, supplemented by boundary friction as the result of any asperity interactions has shown reasonable agreement with the measurements. Both predictions and measurements show that the contribution of compression ring is most significant in the high pressure part of the engine cycle and at top centre reversal between compression and expansion strokes. This indicates that the compression ring complies with its primary sealing function. Viscous friction of the lubricant dominates under the tested and simulated isothermal motored conditions. This in fact is representative of idle to low-speed cycling in creeping traffic with a *cold* engine (conditions which typically form a part of steady-state New European Drive Cycle (NEDC) for emission testing). In addition, the conditions also replicate that of a deactivated cylinder in engines using CDA. The next stage of this research is to include the thermal effects in the analysis and undertake measurement and simulation for steady-state hot engine cycle at simulated low crawling speeds (another part of the NEDC). It is anticipated that boundary friction would play a more significant role under such conditions.

Declaration of Conflicting Interests

The author(s) declared no potential conflicts of interest with respect to the research, authorship, and/or publication of this article.

Funding

The author(s) disclosed receipt of the following financial support for the research, authorship, and/or publication of this article: The authors would like to express their gratitude to the Engineering and Physical Sciences Research Council (EPSRC) for the sponsorship of this research under the Encyclopaedic Program Grant (www.encyclopaedic.org).

References

1. Tung SC and McMillan ML. Automotive tribology overview of current advances and challenges for the future. *Tribol Int* 2004; 37: 517–536.
2. Fitzsimons B. Introduction to the importance of fuel efficiency and role of the encyclopaedic research project. IMechE Seminar on A Drive for Fuel Efficiency, Loughborough, UK, 2011.
3. Andersson BS. Company's perspective in vehicle tribology. In: Dowson D, Taylor CM and Godet M (eds) *Proceedings of 18th Leeds-Lyon symposium*, Elsevier, pp.503–506.
4. Richardson DE. Review of power cylinder friction for diesel engines. *Trans ASME, J Eng Gas Turbines Power* 2000; 122: 506–519.
5. Balakrishnan S, Howell-Smith S and Rahnejat H. Investigation of reciprocating conformal contact of piston skirt-to-surface modified cylinder liner in high performance engines. *Proc IMechE, Part C: J Mechanical Engineering Science* 2005; 219: 1235–1247.
6. Ryk G and Etsion I. Testing piston rings with partial laser surface texturing for friction reduction. *Wear* 2006; 261: 792–796.

7. Rahnejat H, Balakrishnan S, King PD, et al. In-cylinder friction reduction using a surface finish optimization technique. *Proc IMechE, Part D: J Automobile Engineering* 2006; 220: 1309–1318.
8. Rahmani R, Shirvani A and Shirvani H. Optimised textured surfaces with application in piston-ring/cylinder liner contact. In: H Rahnejat (ed.) *Tribology and dynamics of engine and powertrain: Fundamentals, applications and future trends*. London: Woodhead Publishing Ltd., 2010, pp.470–517.
9. Furuhama S and Sasaki S. New device for the measurement of piston frictional forces in small engines. SAE Paper No. 831284, 1983.
10. Gore M, Howell-Smith S, King PD, et al. Measurement of in-cylinder friction using the floating liner principle. In: *Proceedings ASME 2012 internal combustion engine division spring technical conference (ICES 2012)*, Turin, Italy, 6–9 May 2012, Paper No. ICES2012-81028.
11. Gore M, Theaker M, Howell-Smith S, et al. Direct measurement of piston friction of internal combustion engines using the floating liner principle. *Proc IMechE, Part D: J Automobile Engineering* 2014; 228: 344–354.
12. Haddad SD and Tjan K-T. An Analytical study of offset piston and crankshaft designs and the effect of oil film on piston slap excitation in a diesel engine. *Mech Mach Theory* 1995; 30: 271–284.
13. Gohar R and Rahnejat H. *Fundamentals of tribology*. London: Imperial College Press, 2008.
14. Sawicki JT and Yu B. Analytical solution of piston ring lubrication using mass conserving cavitation algorithm. *Tribol Trans* 2000; 43: 587–594.
15. Morris N, Rahmani R, Rahnejat H, et al. The influence of piston ring geometry and topography on friction. *Proc IMechE, Part J: J of Engineering Tribology* 2013; 227: 141–153.
16. Greenwood JA and Tripp JH. The contact of two nominally rough surfaces. *Proc IMechE, Part C: J Mechanical Engineering Science* 1971; 185: 625–633.
17. Morris N, Rahmani R, Rahnejat H, et al. Tribology of piston compression ring conjunction under transient thermal mixed regime of lubrication. *Tribol Int* 2013; 59: 248–258.
18. Shahmohamadi H, Rahmani R, Rahnejat H, et al. Thermo-mixed hydrodynamics of piston compression ring conjunction. *Tribol Lett* 2013; 51: 323–340.
19. Mishra PC. Tribodynamic modeling of piston compression ring and cylinder liner conjunction in high-pressure zone of engine cycle. *Int J Adv Manuf Technol* 2013; 66: 1075–1085.
20. Rahmani R, Theodossiades S, Rahnejat H, et al. Transient elastohydrodynamic lubrication of rough new or worn piston compression ring conjunction with an out-of-round cylinder bore. *Proc IMechE, Part J: J Engineering Tribology* 2012; 225: 284–305.
21. Theaker M, Rahmani R and Rahnejat H. Prediction of ring-bore conformance and contact condition and experimental validation. In: *ASME 2012 International engine division spring technical conference (ICES 2012)*, Torino, Italy, 6–9 May 2012, Paper No. ICES2012-81021.
22. Tian T, Noordzij LB, Wong VW, et al. Modelling piston-ring dynamics, blowby, and ring-twist effects. *Trans ASME, J Eng Gas Turbines Power* 1998; 120: 843–854.
23. Baker CE, Rahnejat H, Rahmani R, et al. Analytical evaluation of fitted piston compression ring: modal behaviour and frictional assessment. SAE Paper No. 2011-01-1535, 2011.
24. Baker CE, Theodossiades S, Rahnejat H, et al. Influence of in-plane dynamics of thin compression rings on friction in internal combustion engines. *Trans ASME, J Eng Gas Turbines Power* 2012; 134: 092801-11.
25. Ma M-T, Sherrington I and Smith EH. Analysis of lubrication and friction for a complete piston-ring pack with an improved oil availability model - Part 1: circumferentially uniform film. *Proc IMechE, Part J: J Engineering Tribology* 1997; 211: 1–15.
26. Bolander NW, Steenwyk BD, Sadeghi F, et al. Lubrication regime transitions at the piston ring-cylinder liner interface. *Proc. IMechE, Part J: J Engineering Tribology* 2005; 219: 19–31.
27. Mishra PC, Rahnejat H and King PD. Tribology of the ring-bore conjunction subject to a mixed regime of lubrication. *Proc IMechE, Part C: J Mechanical Engineering Science* 2009; 223: 987–998.
28. Mishra PC. Modeling the root causes of engine friction loss: Transient elastohydrodynamics of a piston subsystem and cylinder liner lubricated contact. *Appl Math Model* 2014. DOI: 10.1016/j.apm.2014.10.011.
29. Rahnejat H. *Multi-body dynamics: Vehicles, machines and mechanisms*. Bury, St Edmunds: Professional Engineering Publishing, 1998.
30. Vijayaraghavan D and Keith Jr TG. Development and evaluation of a cavitation algorithm. *Tribol Trans* 1989; 32: 225–233.
31. Elrod HG. A cavitation algorithm. *Trans ASME, J Lubric Technol* 1981; 103: 350–354.
32. De la Cruz M, Chong WWF, Teodorescu M, et al. Transient mixed thermo-elastohydrodynamic lubrication in multi-speed transmissions. *Tribol Int* 2012; 49: 17–29.
33. Dowson D and Higginson GR. A numerical solution to the elastohydrodynamic problem. *J Mech Eng Sci* 1959; 10: 6–15.
34. Yang P, Cui J, Jin ZM, et al. Transient elastohydrodynamic analysis of elliptical contacts. Part 2: Thermal and Newtonian lubricant solution. *Proc IMechE, Part J: J Engineering Tribology* 2005; 219: 187–200.
35. Houpert L. New results of traction force calculations in elastohydrodynamic contacts. *Trans ASME, J Tribology* 1985; 107: 241–248.
36. Bin Chik A and Fessler H. Radial pressure exerted by piston rings. *J Strain Anal* 1966; I: 165–171.
37. Teodorescu M, Balakrishnan S and Rahnejat H. Integrated tribological analysis within a multi-physics approach to system dynamics. *Tribol Interf Eng Ser (Elsevier)* 2005; 48: 725–737.
38. Styles G, Rahmani R, Rahnejat H, et al. In-cycle and life-time friction transience in piston ring–liner conjunction under mixed regime of lubrication. *Int J Engine Res* 2014; 15: 862–876.
39. Styles G, Rahmani R, Rahnejat H, et al. Assessment of asperity coefficient of friction for various coating materials used in piston ring/liner conjunction using AFM. In: *15th Nordic symposium on tribology (NORDTRIB 2012)*, Trondheim, Norway, 12–15 June 2012.

40. Eyring H. Viscosity, plasticity and diffusion as examples of absolute reaction rates. *J Chem Phys* 1936; 4: 283–289.
41. Kogut L and Etsion I. Adhesion in elastic-plastic microcontact. *J Colloid Interf Sci* 2003; 261: 372–378.
42. Chong WWF, Teodorescu M and Rahnejat H. Nanoscale elastoplastic adhesion of wet asperities. *Proc IMechE, Part J: J Engineering Tribology* 2013; 227: 996–1010.
43. Perera MSM, Theodossiades S and Rahnejat H. Elasto-multi-body dynamics of internal combustion engines with tribological conjunctions. *Proc IMechE, Part K: J of Multi-body Dynamics* 2010; 224: 261–277.

Appendix

Notation

a, b	front and rear coordinates of piston ring/cylinder liner contact
a_l	acceleration of floating liner
A	piston ring/cylinder liner contact area
A_a	total contact area at the tip of asperities of two opposing surfaces
c	cavitation (film rupture) point
C_1 to C_4	integration constants
E'	composite elasticity modulus
EI	piston ring flexural rigidity
f	total friction
f_b	boundary friction
f_v	viscous friction
F	total force applied on the ring liner contact
$F_2, F_{5/2}$	statistical functions
F_G	gas force on the back of the ring
F_T	ring elastic tension force
g	switching parameter
G	ring end gap at free state
h	film thickness
h_{min}	minimum film thickness
h_s	ring face profile
ℓ	connecting rod length
M	floating liner mass
N	total number of computational segments
p	pressure
p_e	elastic pressure
P_{atm}	atmospheric pressure
P_G	in-cylinder gas pressure
P_s	gas force at the upper rim of the floating liner
r	film reformation point
r_0	bore radius
r_{cr}	crank pin radius
R	radius of curvature for ring face
s, s'	intermediate integration variables
S_0, Z	viscosity constants
t	time
T	temperature
T_0	ambient temperature
U	piston velocity
W	total load supported by contact
W_a	load supported by asperities
W_h	hydrodynamic load
x	Cartesian coordinate
α_0	atmospheric viscosity-pressure coefficient
β_0	atmospheric viscosity-temperature coefficient
β	bulk modulus of elasticity
χ	numerical damping factor
η	dynamic viscosity
η_0	dynamic viscosity at atmospheric pressure
γ	thermal expansion coefficient
κ	average radius of curvature of asperity tips
λ	Stribeck oil film parameter
ω	engine speed
φ	crank angle
ρ	density
ρ_0	density at atmospheric conditions
σ	standard deviation of composite surface roughness of the counterface surfaces
ς	coefficient of asperity shear strength
τ_v	viscous shear stress
τ_0	Eyring shear stress
θ	film ratio
ζ	number of asperity peaks per unit area

Subscripts

a, b	at the ring edges
c	at the cavitation (lubricant film rupture) point
r	at the film reformation point
i	rid index